Chapter 11
The Role of Cavitation in Creep-Fatigue Interaction

Abstract There are many empirical models for the development of creep and fatigue damage. The perhaps most well-known ones are Robison's and Miner's damage summation rules. They are based on the mechanical behavior during monotonous and cyclic loading. To improve the accuracy of the damage assessment, it is important to analyze the changes in the microstructure as well, not least the cavitation. To describe cyclic loading, special empirical models have often been used in the past, some with numerous adjustable parameters. Recently, a model for cyclic loading has been formulated that is based on the corresponding expressions for monotonous loading. The main change is that the value of the dynamic recovery constant is increased. In this way, cyclic hysteresis loops can be reproduced without adjustable parameters. Cavitation is believed to be of the same technical importance during cyclic as during static loading. In spite of this, the number of studies of cavitation during cyclic loading is quite limited. One set of data exists for a 1Cr0.5Mo steel. The static cavitation models have been transferred to cyclic conditions. It is demonstrated that these models can describe the cavitation both during low cycle fatigue (LCF) and combined creep and LCF.

11.1 General

High temperature plants are often exposed to a combination of creep and fatigue. A common feature is thermal fatigue where components are exposed to straining during start-ups and shut-downs. During operation primary stresses (direct loading) as well as secondary stresses (self-equilibrium stresses) appear that give rise to creep damage. Although some types of plants like steam and gas turbines are particularly exposed to cyclic loading, both creep and fatigue are of importance in many plants. In recent years significant contributions from solar and wind power have been added to the electric supply. Since the amount of power of these renewable sources depends on the weather, additional basic power is needed. This has implied that many fossil fired power plants have been put into standby and are operated intermittently. This

© The Author(s) 2024

R. Sandström, *Basic Modeling and Theory of Creep of Metallic Materials*, Springer Series in Materials Science 339,
https://doi.org/10.1007/978-3-031-49507-6_11

means that number of start-ups and shut-downs are increased and thereby the amount of cyclic loading.

Different types of damage appear depending on the relative amounts of creep and fatigue. If there is limited creep due to short loading times at high temperatures, the life time is controlled by fatigue [1]. Pure fatigue is dominated by transgranular crack initiation, Fig. 11.1a. On the other hand if there is modest amount of fatigue, the damage will be dominated by creep. Creep gives rise to cavitation in the grain boundaries, Fig. 11.1b. If fatigue and creep take place sequentially, the main cracks changes from transgranular to intergranular, Fig. 11.1c. If creep and fatigue loading occur simultaneously, the creep damage in the grain boundaries provides easy paths for the fatigue cracks, Fig. 11.1d.

Creep-fatigue interactions have traditionally been studied with low cycle fatigue (LCF) at a temperature close to the maximum operation temperature [3]. To observe any influence of creep, it is essential to include hold times in the load cycles [1]. However, it has turned out that LCF typically gives a lower amount of damage than is found in components. For simulating the role of straining during start-ups and shut-downs, thermal mechanical fatigue (TMF) is often used where both the loading and temperature are varied during the cycle. It is important that the minimum temperature in the cycle is low, since a significant part of the damage is generated at low temperatures [4]. LCF and TMF are commonly performed under strain control. A number of tests are carried out with a sequence of different maximum strains in the cycles. Hold times are introduced at the maximum and/or minimum strains. During

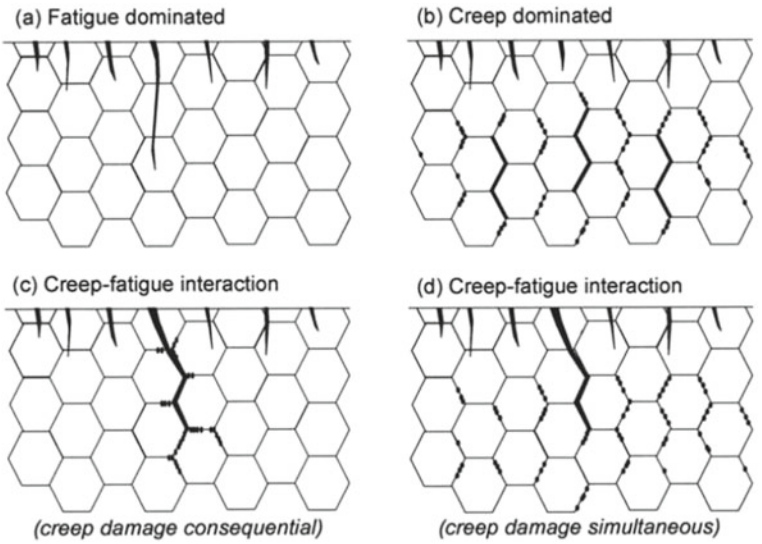

Fig. 11.1 Appearance of creep-fatigue damage mechanisms; **a** fatigue controlled; **b** creep controlled; **c** creep-fatigue interaction (sequential); **d** creep-fatigue interaction (simultaneous). Reprinted from [2] with permission of Taylor & Francis

the hold times the strain level is fixed during which the stress is relaxing due to creep. An alternative is to have hold times at a fixed stress. Since the absolute value of the average stress is larger during the hold times in this case, it gives rise to more creep damage than for a hold time at constant strain. The amount of creep damage can be increased by raising the length of the hold time or by lowering the strain rate in the cycle.

It is well-known that formation of creep cavities plays an important role during creep-fatigue interaction. This is illustrated in Fig. 11.1. In spite of the importance of creep cavities during creep-fatigue, only limited efforts to generate basic modeling of the phenomenon have been taken [5]. Instead, reference has to be made to brittle creep rupture during static conditions. It can be assumed that many of the mechanisms are similar for cyclic and static loading. The main mechanism for creep damage is believed to be initiation and growth of creep cavities in the grain boundaries. When the cavitated area fraction in the grain boundaries has reached a certain level, cracks are formed and rupture is close in common specimens [6]. In larger specimens and components the crack propagation stage is also of major importance [7].

Grain boundary sliding (GBS) is commonly assumed to give rise to cavity formation. This is a natural assumption. Considering for example particles in the grain boundaries. GBS will generate extensive shearing around the particles that can easily initiate cavities. However, cavities can also be formed in grain boundaries where very few particles are present such as in pure copper. Lim provided a model for this situation by taking into account the presence of substructure [8]. Cavities can form at the intersection between grain boundaries and the substructure. He showed that this process is thermodynamically feasible and there is an energy gain when cavities are formed. Quantitative models for cavity nucleation could now be formulated.

It has been shown experimentally and with the help of finite element methods (FEM) that the amount GBS is proportional to the creep strain [8, 9]. The FEM modeling also gives the proportionality constant, so it can be used for quantitative predictions. Using these findings and the assumption that cavities can nucleate at particles and subgrain-grain boundary junctions, the double ledge model was formulated [10]. This model gives that the number of cavities is proportional to the creep strain and the results are in quantitative agreement with observations [11]. It is assumed that these principles can be taken over for cyclic loading, Sect. 11.4.

Models for diffusion controlled growth of creep cavities have been available for many years. Unfortunately, these models typically predict much higher growth rates than the observed ones. It was however realized that cavities inside a material (not on the surface) cannot grow faster than the creep rate of the surrounding material. This is referred to as constrained growth in contrast to the unconstrained models [12]. Models for constrained growth were quickly developed and gave a better agreement with observations, see for example [13]. The models still tended to overestimate the growth rate. For this reason, the models were reanalyzed and with the help of FEM studies. A new and improved model could be established that is in better agreement with experiments [14].

Strain controlled growth of creep cavities can also take place in addition to diffusion growth. There are number of models based on plastic straining in the literature.

Unfortunately, most of these models do not consider constrained growth contrary to the situation for diffusion growth, which means that the predicted grow rate can give quite large cavity growth during creep. Recently, a model that takes the criterion for constraint growth into account has been presented which is of importance during creep [5]. During cyclic deformation, constrained cavity growth is not expected to be significant due to the often small creep strain in the cycles. This will be discussed in Sect. 11.4.2.

For creep failure it is important to distinguish between ductile and brittle rupture. Ductile rupture has been shown to occur after ductility exhaustion or after plastic instability has taken place (in specimens necking) [15]. Brittle rupture in many engineering materials takes place after the cavitated area fraction in the grain boundaries has reached a certain level. To predict creep rupture, the development of the microstructure must be possible to model including the dislocation structure, particle structure and the fraction of elements in solid solution. In this way the dislocation strengthening, particle hardening and solid solution hardening can be computed. In addition, quantitative models for cavity nucleation and growth must be available. Such models have been established and the creep rupture behavior has successfully been predicted for austenitic stainless steels without the use of adjustable parameters, see for example [16].

For monotonous loading these principles are well established. However, data and parameter values cannot be applied to cyclic loading directly and basic models for this case are only available to a limited extent. For example, the value of the dynamic recovery constant is much larger during cyclic than during static loading [5]. This will be analyzed in Sect. 11.3. Models for cavitation during low cycle fatigue will be presented in Sect. 11.4 and compared to experimental data for 1Cr0.5Mo steel.

11.2 Empirical Principles for Development of Creep-Fatigue Damage

11.2.1 Fatigue and Creep Damage

Basic models for describing creep rupture are available. Several models have been given in this book. However, for cyclic loading basic models do not seem to have been developed. However, many empirical models can be found. A model that is applicable to many materials is the Coffin-Manson equation

$$N_{\text{init}} = C_{\text{CM}}(\Delta\varepsilon_{\text{pl}})^{-\beta_{\text{CM}}} \tag{11.1}$$

where N_{init} is the number of cycle to crack initiation and $\Delta\varepsilon_{\text{pl}}$ the plastic strain range in the load cycle. C_{CM} and β_{CM} are constants that are fitted to the observations. Equations of type in (11.1) can sometimes also be used for the elastic and total strain range. The use of Eq. (11.1) is illustrated in Fig. 11.2.

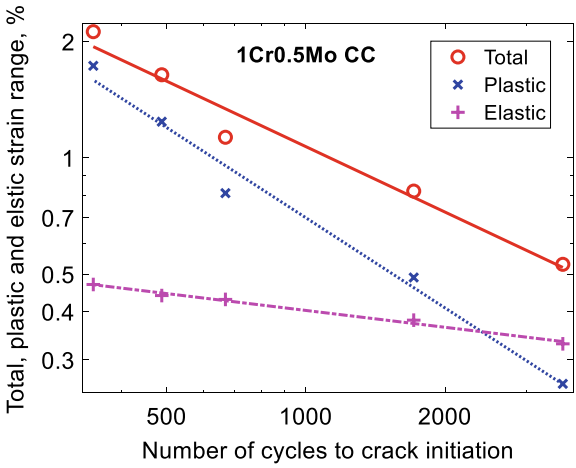

Fig. 11.2 Relation between the number of cycles to crack initiation and the total, plastic and elastic strain ranges for 1Cr0.5Mo during continuous cycling (CC). Experimental data from [17]. Redrawn from [18] with permission of Taylor & Francis

The influence of pre-creep before LCF and/or hold time during the LCF is illustrated in Fig. 11.3. With increasing amount of creep, the elastic strain range at a given number of cycles to crack initiation is significantly reduced. However, the effect of creep on the plastic strain range relation is not very pronounced.

The total fatigue damage D_F is often determined with the help of Miner's law. It is based on linear summation of the damage over individual cycles

$$D_F = \sum_i \frac{n_i}{N_{init}(\Delta\varepsilon_{pl}(i))} \tag{11.2}$$

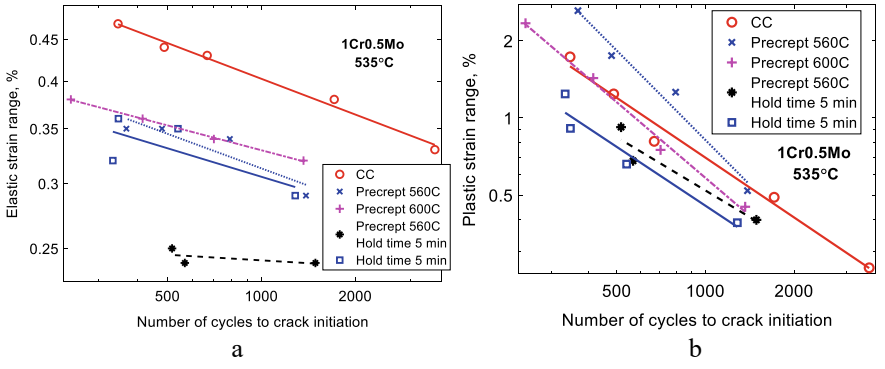

Fig. 11.3 Influence of 5% pre-creep strain and/or 5 min hold time on the number of cycles to crack initiation as a function of strain range for 1Cr0.5Mo. Experimental data from [17]; **a** elastic strain range; **b** plastic strain range

where n_i is the number of cycles when the plastic strain range is $\Delta\varepsilon_{pl}(i)$ giving a number of cycles to crack initiation of $N_{init}(\Delta\varepsilon_{pl}(i))$. When the damage reaches unity, failure is assumed to take place.

There are many expressions for the creep damage D_C. The classical principle is based on linear time fractions (Robinson rule)

$$D_C = \int_0^t \frac{dt_1}{t_R(T(t_1), \sigma(t_1))} \tag{11.3}$$

where $t_R(T, \sigma)$ is the rupture time at temperature T and stress σ as a function of time t. An alternative way is to base the damage on ductility exhaustion

$$D_C = \int_0^t \frac{\frac{d\varepsilon}{dt}(T(t_1), \sigma(t_1))dt_1}{\varepsilon_R(T(t_1), \sigma(t_1))} \tag{11.4}$$

where the accumulated creep strain is compared to the rupture ductility. A simple assumption of how to combine D_F and D_C would be to just add them. This means that rupture is predicted to occur when

$$D_F + D_C = 1 \tag{11.5}$$

However, detailed experiments have shown that such a relation is not conservative enough. In fact, bilinear equations have been demonstrated to agree with observations and have also been standardized by ASME

$$\begin{aligned} D_F &= 1 - \frac{1-\alpha_{FC}}{\alpha_{FC}} D_C \quad D_F \geq D_C \\ D_C &= 1 - \frac{1-\alpha_{FC}}{\alpha_{FC}} D_F \quad D_C \geq D_F \end{aligned} \tag{11.6}$$

The constant α_{FC} has been found to be material dependent. Holdsworth [7] gives the following values: for the austenitic stainless steels 18Cr10Ni and 17Cr12Ni2Mo, $\alpha_{FC} = 0.33$, for 20Cr30NiTi, $\alpha_{FC} = 0.11$, for 9Cr1Mo (P91), $\alpha_{FC} = 0.25$ and for 2.25Cr1Mo, $\alpha_{FC} = 0.11$. The bilinear relation in Eq. (11.6) is illustrated in Fig. 11.4. For comparison Eq. (11.5) would give a straight line between (0, 1) and (1, 0). Equation (11.6) is thus considerably more conservative than Eq. (11.5).

For plain specimens of parent metal, Eq. (11.6) is very well supported. However, already by considering multi-axial stresses, the prediction of the rupture time in Eq. (11.3) becomes an issue. Hayhurst [19] proposed that the rupture stress σ_R under multi-axial conditions could be represented by

$$\sigma_R = \gamma_1\sigma_1 + \gamma_2\sigma_h + \gamma_3\sigma_e \tag{11.7}$$

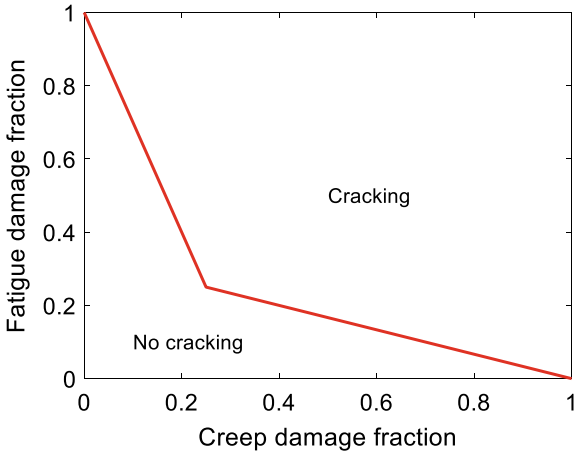

Fig. 11.4 Bilinear criterion for failure with combined fatigue and creep damage according to Eq. (11.6) with $\alpha_{FC} = 0.25$. Below the criterion line no cracking should take place

where σ_1 is the maximum principal stress, σ_h the average of the principal stresses and σ_e the effective stress. γ_1, γ_2 and γ_3 are constants that are fitted to creep rupture data under multi-axial conditions. It has been shown that Eq. (11.7) can be used to describe experimental data in a number of cases. However, it turns out that different authors give different values for γ_1, γ_2 and γ_3. Since the results of Eq. (11.7) are very sensitive to the values of these constants, it is difficult to use Eq. (11.7) to estimate the rupture stress. The issues with Eq. (11.7) have been discussed by Wen et al. [20]. This is one of the reasons why the ductility exhaustion expression for creep damage Eq. (11.4) is preferred by many authors to the estimate of the damage by integration over the rupture time, Eq. (11.3) [2]. The influence of multiaxiality on the creep rate can be described directly with the Odqvist equation [21]

$$\dot{\varepsilon}_{ij} = \frac{3}{2}\frac{s_{ij}}{\sigma_e}h(\sigma_e) \tag{11.8}$$

The stress dependence of the creep rate $h(\sigma)$ in the secondary stage can be found in Eq. (5.31). The stress deviator s_{ij} and the effective stress σ_e are given by

$$s_{ij} = \sigma_{ij} - \sigma_h\delta_{ij} \tag{11.9}$$

$$\sigma_e = \sqrt{\left((\sigma_1 - \sigma_2)^2 + (\sigma_2 - \sigma_3)^2 + (\sigma_3 - \sigma_1)^2\right)/2} \tag{11.10}$$

where σ_{ij} is the stress tensor, δ_{ij} the Kronecker delta, σ_1, σ_2 and σ_3 the principal stresses, and σ_h the hydrostatic stress (the average of the principal stresses). i and j runs over the coordinate directions 1, 2 and 3. By considering uniaxial conditions ($\sigma_1 = \sigma$, $\sigma_2 = \sigma_3 = 0$), it can easily be shown that the expected creep rates $\dot{\varepsilon}_{11} = \dot{\varepsilon}_u$, $\dot{\varepsilon}_{22} = -\dot{\varepsilon}_u/2$, $\dot{\varepsilon}_{33} = -\dot{\varepsilon}_u/2$ are reproduced, where $\dot{\varepsilon}_u$ is the uniaxial creep rate.

For the creep ductility, the influence of multiaxiality has been characterized quite well and there is a fair agreement between several models and experiments at least for notched bars. This is analyzed in Sect. 13.4.4. For example, the model by Wen and Tu seems to represent many sets of experimental data [22].

In the paper by Wen et al. [20] it is quite well documented that ductility exhaustion, Eq. (11.4) gives a considerably safer prediction than that based on the life fraction rule, Eq. (11.3). Even for ductility exhaustion, they demonstrate that the predicted damage typically deviates a factor of three up or down.

These results confirm many earlier results that it is not safe to base damage estimates solely on mechanical properties. It is also important to predict the microstructure development in terms of particle coarsening, subgrain growth, cavitation, etc. and compare the findings with observations. If it can be done with continuum damage mechanics that is fine, but it is strongly recommended to use basic models of the type formulated in this book.

A third way to estimate the damage is to compute the cavitated area fraction A_{cav} in the grain boundaries (Eq. (13.8))

$$A_{\text{cav}} = \int_0^t \frac{dn_{\text{cav}}}{dt'}(t')\pi R_{\text{cav}}^2(t,t')dt' \tag{11.11}$$

where n_{cav} is the number of creep cavities per unit grain boundary area and R_{cav} their radius. The amount of damage is then

$$D_{\text{C}} = A_{\text{cav}}/A_{\text{cavcrit}} \tag{11.12}$$

A_{cavcrit} is the amount of cavitation when cracks are initiated. If it is possible to record the cavitation, it is usually the safest way to assess the amount of damage. The modeling of n_{cav} and R_{cav} during cyclic loading is handled in Sect. 11.4.

11.2.2 Loops During Cyclic Loading

During cyclic loading the stress versus strain curves form loops that are called hysteresis loops. Perhaps the most common way of describing a hysteresis loop is with the Ramberg-Osgood equation

$$\varepsilon_{\text{a}} = \frac{\sigma_{\text{a}}}{E} + \left(\frac{\sigma_{\text{a}}}{K_{\text{lp}}}\right)^{\gamma_{\text{lp}}} \tag{11.13}$$

where ε_{a} is the strain, σ_{a} is stress, and E the elastic modulus. K_{lp} and γ_{lp} are adjustable parameters that are fitted to the experimental data. There are more complex approaches based on the assumption that the loops are due to the build-up of residual

stresses. The first such approach was due to Masing but models based on the superposition of a distribution of yield strengths have also been proposed [23].

The creep damage in a stress strain loop is primarily due to the stress relaxation during a hold time and thereby the amount of creep strain. To describe the stress relaxation during a hold time, the Feltham equation is often used for this purpose

$$\sigma_{\text{rel}} = \sigma_{\text{st}}(1 - \sigma_0 B_{\text{rel}} \log(1 + b_{\text{rel}} t)) \tag{11.14}$$

where σ_{st} is the start stress, σ_{rel} is the stress after relaxation and t the relaxation time. B_{rel}, b_{rel} and σ_0 are adjustable parameters. References to the original papers can be found in [24] where also some applications of the equations are given.

11.3 Deformation During Cyclic Loading

11.3.1 Basic Model for Hysteresis Loops

Empirical models for representing hysteresis loops are readily available. A few examples were mentioned in Sect. 11.2.2. Adjustable parameters in these models are fitted to the experimental data. Often a reasonable fit to the data can easily be obtained. There are however drawbacks with the empirical approaches. Typically a good fit can be found with many mathematical expressions and then it is difficult to know which one represents the correct mechanism. It is practically always desirable to extrapolate the results to new condition but if the operating mechanisms are not safely identified, generalization of the results becomes quite uncertain unless a large set of experimental data is available. Phrased in another way, empirical models are not predictable.

For creep under non-cyclic conditions, basic models have been presented in several chapters in the book and also in publications, for a survey, see [25]. The models are formulated from basic physical principles and have been shown to reproduce experimental data for copper, aluminum and austenitic stainless steels in a satisfactory way without using adjustable parameters. Such models are referred to as basic in this book. Only limited attempts have been made to perform the corresponding derivation for cyclic deformation, which involves elastic, plastic and creep deformation. The procedure described in [5] will be followed. The Voce equation can describe the plastic flow curve for a number of materials. This equation is given in Eq. (3.14) and can also be found in [26].

$$\sigma = \sigma_y + (\sigma_{\text{max flow}} - \sigma_y)(1 - e^{-\omega \varepsilon_{\text{pl}}/2}) \tag{11.15}$$

where σ is the applied stress, ε_{pl} the plastic strain, σ_y the yield strength, $\sigma_{\text{max flow}}$ the maximum flow stress, and ω the dynamic recovery constant. The deviation from linear behavior of the work hardening is controlled by ω. The plastic strain rate can

be obtained from Eq. (11.15)

$$\frac{d\varepsilon_{\mathrm{pl}}}{dt} = \frac{2}{\omega(\sigma_{\max\,\mathrm{flow}} - \sigma)}\frac{d\sigma}{dt} \tag{11.16}$$

The creep rate in the secondary stage $\dot{\varepsilon}_{\mathrm{sec}}$ is given in Eq. (4.3). The original derivation can be found in [27]

$$h(\sigma) = \frac{2bc_{\mathrm{L}}}{m_{\mathrm{T}}}\frac{D_{\mathrm{self0}}b\tau_L}{k_{\mathrm{B}}T}\left(\frac{\sigma}{\alpha Gb}\right)^3 e^{\frac{\sigma b^3}{k_{\mathrm{B}}T}} e^{-\frac{Q_{\mathrm{self}}}{R_{\mathrm{G}}T}\left[1-\left(\frac{\sigma}{\sigma_{\mathrm{imax}}}\right)^2\right]} e^{-\frac{Q_{\mathrm{sol}}}{RT}} \tag{11.17}$$

$$\frac{d\varepsilon_{\mathrm{sec}}}{dt} = h(\sigma - \sigma_{\mathrm{i}}) \tag{11.18}$$

where T is the absolute temperature, σ the applied stress, D_{s0} the pre-exponential coefficient for self-diffusion, Q_{self} the activation energy for self-diffusion, k_{B} Boltzmann's constant, R_{G} the gas constant, m_{T} the Taylor factor, b Burger's vector, τ_{L} the dislocation line tension, σ_{imax} the maximum flow stress, and c_{L} a work hardening constant. Solid solution hardening gives an additional contribution Q_{sol} to the activation energy. σ_{i} is an internal stress that includes contributions from solid solution hardening and particle hardening. The stress exponent is about 3 at low stresses, but increases rapidly with increasing stress. According to Eq. (4.6), the primary creep rate is given by

$$\frac{d\varepsilon_{\mathrm{prim}}}{dt} = h(\sigma + \sigma_{\mathrm{disl\,sec}} - \sigma_{\mathrm{disl}} - \sigma_{\mathrm{i}}) \tag{11.19}$$

In comparison to (11.18) an extra stress has been introduced

$$\sigma_{\mathrm{prim}} = \sigma_{\mathrm{disl\,sec}} - \sigma_{\mathrm{disl}} \tag{11.20}$$

For this model for primary creep that was described in Sect. 4.3, primary creep is fully accounted for just by introducing the extra stress in Eq. (11.20). It is the difference between the dislocation stress in the secondary stage $\sigma_{\mathrm{disl\,sec}}$ and that in the primary stage σ_{disl}. Since the dislocation density in the primary stage is normally much lower than that in the secondary stage, consequently $\sigma_{\mathrm{disl\,sec}}$ is much higher than σ_{disl}. The result is that the creep rate is much higher in the primary stage than in the secondary stage as it should. This is also directly evident from Eq. (11.19).

In a hysteresis loop, the stress is not stationary but varies all the time. It goes through the cycle so the creep process is restarted in every half cycle. This means that primary creep is involved. But in fact, Eq. (11.18) is still valid [28]. This can be seen from Eqs. (11.20) and (11.21). In these equations, $\sigma + \sigma_{\mathrm{prim}}$ correspond to the stress during cyclic loading. The result is simply

$$\frac{d\varepsilon_{\mathrm{prim}}}{dt} = h(\sigma - \mathrm{sgn}(\dot{\varepsilon}_{\mathrm{tot}})\sigma_{\mathrm{i}}) \tag{11.21}$$

This equation is obviously identical to Eq. (11.18) apart from the different sign in front of σ_i in the compression and the tension going part of the cycle.

The total strain rate $\dot{\varepsilon}_{tot}$ has contributions from the elastic $\dot{\varepsilon}_{el}$, plastic $\dot{\varepsilon}_{pl}$, and creep strain rate $\dot{\varepsilon}_{prim}$. The sum of the elastic, plastic, and creep strain rate is equal to the external strain rate

$$\frac{d\varepsilon_{el}}{dt} + \frac{d\varepsilon_{pl}}{dt} + \frac{d\varepsilon_{prim}}{dt} = \frac{d\varepsilon_{tot}}{dt} \tag{11.22}$$

where the elastic strain rate $\dot{\varepsilon}_{el}$ is

$$\frac{d\varepsilon_{el}}{dt} = \frac{d\sigma}{dt}\frac{1}{E} \tag{11.23}$$

and E is the elastic modulus. By combining Eqs. (11.16), (11.21), (11.22) and (11.23), the stress rate that gives the hysteresis loops is found

$$\frac{d\sigma}{dt} = \frac{1}{1/E + 2/\left[\omega(\sigma_{\max\,flow} - \mathrm{sgn}(\dot{\varepsilon}_{tot})\sigma)\right]}\left[\frac{d\varepsilon_{tot}}{dt} - h(\sigma - \mathrm{sgn}(\dot{\varepsilon}_{tot})\sigma_i)\right] \tag{11.24}$$

The sign function sgn in Eq. (11.21) is necessary to make the equation valid for both the tension and compression going parts of the loop.

When applying Eq. (11.24) for hysteresis loops, the starting point is that the properties used in monotonous loading should be taken over to as large extent as possible. Creep properties can be found for many materials. However, tensile properties at elevated temperatures are often more difficult to locate. The temperature dependence of the maximum flow stress below the creep range is approximately related to that of the elastic modulus (unpublished results)

$$\sigma_{\max\,flow}(T) = \sigma_{\max\,flow}(\mathrm{RT})\left[\frac{E(T)}{E(\mathrm{RT})}\right]^2 \tag{11.25}$$

where T and RT represent the value at temperature and room temperature, respectively. The dynamic recovery constant ω has also a related temperature dependence. But there is also another effect. ω describes how fast dislocations of opposite burgers' vectors on the same slip plane annihilate when they meet. But during cyclic deformation dislocations meet much more frequently that raises the value of ω. Each half cycle in the hysteresis loop can in this respect be considered equivalent to the strain to uniform elongation in the monotonous case. The resulting equation for ω is then

$$\omega(T) = \omega(\mathrm{RT})\frac{\varepsilon_u}{\varepsilon_r}\left[\frac{E(\mathrm{RT})}{E(T)}\right]^2 \tag{11.26}$$

where ε_u is the uniform elongation during monotonous loading and ε_r the strain range during cycling. Observe that the influence of the temperature dependence of the elastic modulus is opposite for $\sigma_{max\ flow}$ and ω.

11.3.2 Application of the Cycling Model

A model for the hysteresis loop is given in Eq. (11.24) based on the same principles as for stationary deformation. Elastic, plastic and creep deformation are considered. It involves parameter values for monotonous loading except for the dynamic recovery constant ω which has to be raised due to the frequent encounter of dislocations during cyclic deformation according to Eq. (11.26).

Equation (11.24) is applied in Fig. 11.5 to the 21Cr11Ni austenitic stainless steel 253 MA, that has rare earth metal additions to improve the oxidation resistance and can therefore be used up to 1000 °C. A loop for continuous cycling is illustrated.

An acceptable description of the loop is obtained. Data for the studied material can be found in [29].

The high value of ω is quite important. If the monotonous value for ω is used ($\omega = 15$ at room temperature) without taking the loop factor $\varepsilon_u/\varepsilon_r$ into account, the observed type of loop cannot be reproduced. This is shown in Fig. 11.6. Obviously, a reasonably formed looped cannot be formed.

In Sect. 11.4 on cavitation, the steel 1Cr0.5Mo will be studied. Since creep rate data for the steel have not been found, the model values have been compared to rupture data assuming that the Monkman-Grant relationship is valid. The rupture data is shown in Fig. 11.7.

An Arrhenius expression is fitted to the data

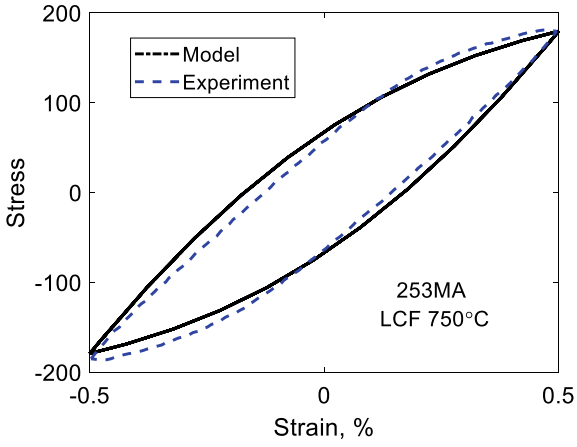

Fig. 11.5 Hysteresis loop for low cycle fatigue (LCF) of the austenitic stainless steel 253 MA at 750 °C. Experimental data are compared with the model in Eq. (11.24). Redrawn from [18] with permission of Taylor & Francis

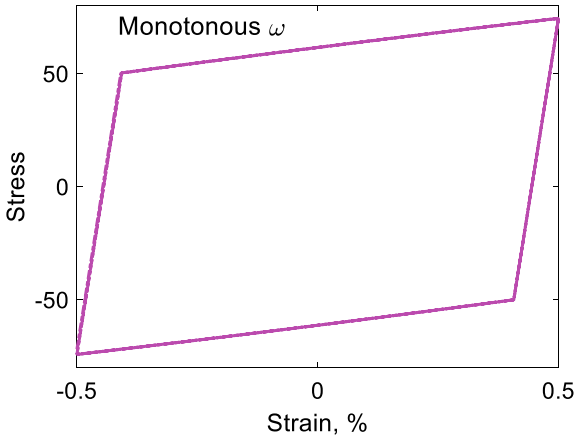

Fig. 11.6 Simulated hysteresis loop for low cycle fatigue (LCF) with the same parameter values except that a low ω (=15 at room temperature) value characteristic of monotonous deformation is used

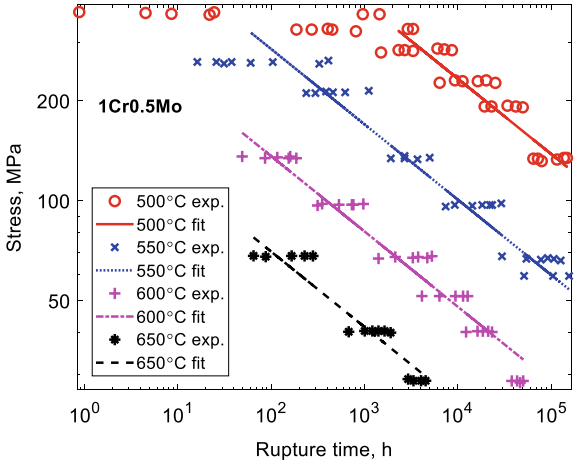

Fig. 11.7 Creep rupture data for 1Cr0.5Mo steel [30] fitted to an Arrhenius expression. Redrawn from [18] with permission of Taylor & Francis

$$\frac{1}{t_R} = C_R \exp\left(-\frac{Q_R}{k_B T}\right)\sigma^{n_N} \tag{11.27}$$

The data for stresses above 300 MPa are ignored since they are not of importance for the hysteresis loops. The values of the constants are $Q_R = 391$ kJ/mol, $n_N = 4.4$ and $C_R = 1.0 \times 10^{12}$ with the rupture time t_R in hours. Equation (11.27) is transferred to strain rate with the help of the modified Monkman-Grant relation.

$$\dot{\varepsilon} = \frac{\varepsilon_R}{t_R} \tag{11.28}$$

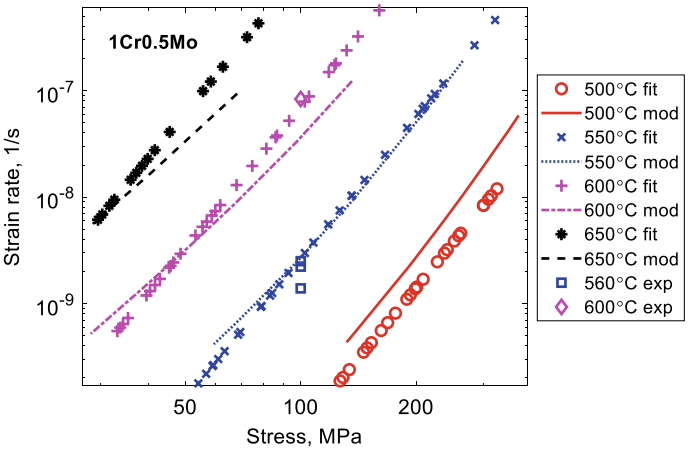

Fig. 11.8 Creep rate model values for 1Cr0.5Mo steel according to Eqs. (11.17) and (11.18) compared creep rupture data [30] fitted to an Arrhenius expression as well as to experimental creep rate values from [17]

The rupture ductility ε_R is taken as 0.1. The strain rate according to the model in Eqs. (11.17) and (11.18) is compared to that in Eq. (11.28) in Fig. 11.8. A few experimental data points for the creep rate from [17] are also included.

A precise agreement in Fig. 11.8 is not to be expected because the Monkman-Grant equation is only an approximate relation. In addition, the activation energy for the rupture is quite high, 390 kJ/mol. This should be compared to the activation energy for self-diffusion for ferrite that is 240 kJ/mol. For the creep rate this value is raised by the contribution from solid solution hardening that has been taken as 50 kJ/mol. The difference in activation energy between creep rupture and rate is still quite significant. The modelled strain rate are anyway of the right order around 550 °C, where the results are used for modeling hysteresis loops.

Four modeled loops for 1Cr0.5Mo steels are compared to experimental data in Figs. 11.9 and 11.10.

In Fig. 11.9, two loops cycled at 535 °C with and without pre-creep are compared. Pre-creep reduces the stress range probably due to softening of the microstructure during the creep process. In Fig. 11.10, the influence of a hold time is illustrated that decreases the stress range further. Pre-creep reduces the stress range also in this case. It is evident that the model in Eq. (11.24) can at least approximately describe the influence of pre-creep and hold time on the hysteresis loops.

To illustrate the applicability of the model in Eq. (11.24) quite a different case where creep has the main influence on the hysteresis loops is considered. This should be contrasted to Figs. 11.9 and 11.10 where the dominant influence on the loops is from cycling. Loops have been computed for alloy PM2000, which is a ferritic oxide dispersion strengthened (ODS) alloy with the approximate composition 20Cr5Al0.4Ti0.5Y2O3 [31]. Loops are presented in Fig. 11.11 at 1200 °C for two different strain rates. The dominance of creep is demonstrated by the flat upper

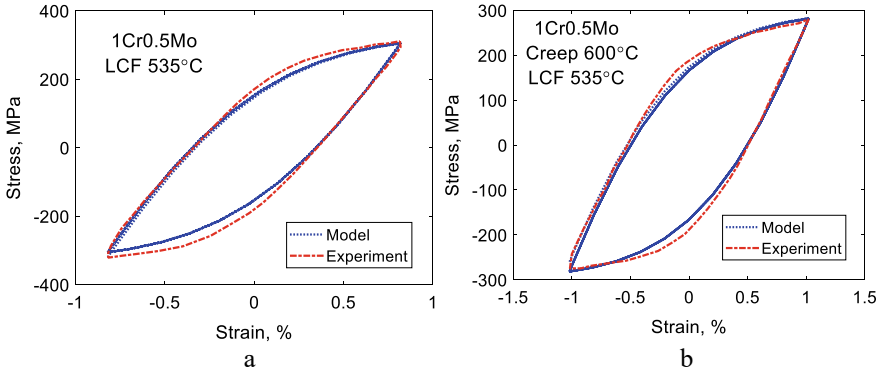

Fig. 11.9 Hysteresis loop for low cycle fatigue (LCF) of the ferritic-bainitic steel 1Cr0.5Mo at 535 °C. Experimental data from [17] are compared with the model in Eq. (11.24). **a** Tempered condition; **b** pre-crept to 5% strain at 600 °C. Redrawn from [18] with permission of Taylor & Francis

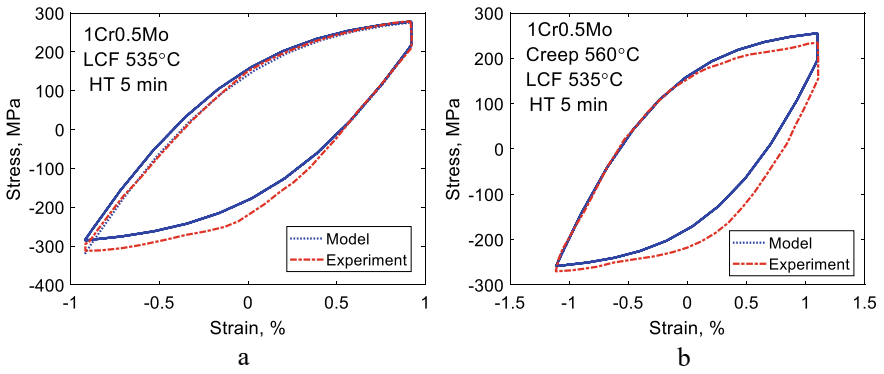

Fig. 11.10 Hysteresis loop for low cycle fatigue (LCF) of the bainitic steel 1Cr0.5Mo at 535 °C with a hold time of 5 min. Experimental data from [17] are compared with the model in Eq. (11.24). **a** Tempered condition; **b** pre-crept to 5% strain at 560 °C. Redrawn from [18] with permission of Taylor & Francis

and lower parts of the loops. The high temperature is the origin of the strong role of creep. The creep strain is of importance at lower stresses. This means that the vertical parts of the loops are controlled by the initial straighter part of the work hardening. The main effect of the lower strain rate in Fig. 11.11b is that it reduces the stress range somewhat.

In Fig. 11.12 a loop for thermo-mechanical fatigue (TMF) is presented. The thermal cycling is between 800 and 1200 °C with strain and temperature in phase, i.e. the maximum strain and temperature appear together. This is quite a severe test of the model in Eq. (11.24). The upper and lower parts of the loop are again controlled by creep. Since the temperature is increasing in parallel to the increasing strain in

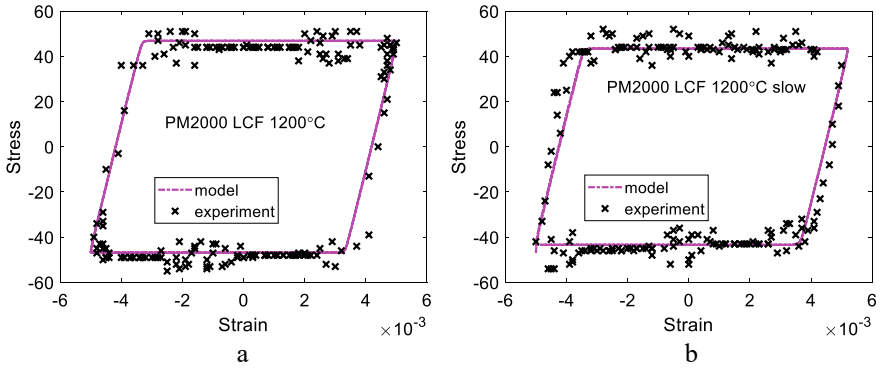

Fig. 11.11 Hysteresis loop for low cycle fatigue (LCF) of the ferritic ODS alloy at 1200 °C. Experimental data from [31] are compared with the model in Eq. (11.24); **a** strain rate 7×10^{-4} 1/s; **b** strain rate 5×10^{-5} 1/s. Reprinted from [5] with permission of Springer

the upper part of the loop, the stress is gradually decreasing. For the same reason the absolute value of the creep stress increases with decreasing strain in the lower part of the loop when the temperature is reduced.

Previously, the loops in Figs. 11.11 and 11.12 have been represented with an empirical model involving a number of adjustable parameters [31]. Such analysis is restricted to measured loops, and generalizing the results, for example, for computation of the fatigue and creep damage is difficult to manage in a safe way. However with the basic model for the hysteresis loop, the situation is different. It has been demonstrated that the model can handle different cases without using adjustable parameters. The possibility to extrapolate the results to new situations is then dramatically improved. In the past it has often been assumed that the shape of the hysteresis loops is due to the presence of a complex state of residual stresses that can be described with the Masing model or a distribution of yield strengths [23]. However, the results

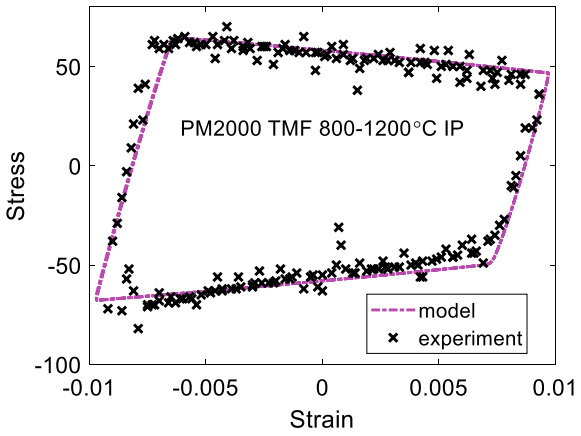

Fig. 11.12 Hysteresis loop for thermo-mechanical fatigue (TMF) of the ferritic ODS alloy PM2000 between 800 and 1200 °C in phase. Strain rate 5×10^{-5} 1/s. Experimental data from [31] are compared with the model in Eq. (11.24). Reprinted from [5] with permission of Springer

in this section demonstrate that monotonous and cyclic loading can be handled in the same way just by modifying the value of the dynamic recovery constant.

11.4 Cavitation

11.4.1 Nucleation of Cavities

The basic principles for nucleation of creep cavities are assumed to be the same in cycling and monotonous loading. Basic mechanisms for nucleation are discussed in 10.4 and in [6]. Although a number of mechanisms for nucleation have been proposed in the literature, the experimental data are fully consistent with the starting point that cavities are formed by grain boundary sliding (GBS). Cavities open up at particles or at subboundary—grain boundary junctions in sliding grain boundaries. The amount of GBS u_{GBS} is proportional to the creep strain, Eq. (9.11)

$$u_{\mathrm{GBS}} = C_{\mathrm{s}}\varepsilon \tag{11.29}$$

The value of the proportionality constant C_{s} has been determined with the help of FEM modeling [32], Eq. (9.12)

$$C_{\mathrm{s}} = \dot{u}_{\mathrm{GBS}}/\dot{\varepsilon} = \frac{3\phi}{2\xi} d_{\mathrm{g}} \tag{11.30}$$

where d_{g} is the grain size, $\phi = 0.15$–0.33 (the value increases with the creep stress exponent) and $\xi \approx 1.4$ are constants. With the help of the so called double ledge model, the nucleation rate can be related to the amount of creep strain [10]. According to this model, nucleation is assumed to take place when a subboundary on one side of a sliding grain boundary meets a subboundary on the other side or a particle. The result is the following nucleation rate, Eq. (10.8)

$$\frac{dn_{\mathrm{cav}}}{dt} = \frac{0.9C_s}{d_{\mathrm{sub}}}\left(\frac{g_{\mathrm{sub}}}{d_{\mathrm{sub}}^2} + \frac{g_{\mathrm{part}}}{\lambda^2}\right)\dot{\varepsilon} = B_{\mathrm{s}}\dot{\varepsilon} \tag{11.31}$$

where n_{cav} is the number of cavities nucleated per unit grain boundary area, and d_{sub} is the subgrain diameter. d_{sub} is inversely proportional to the dislocation stress that is in general close to the applied stress. λ is the interparticle spacing in the grain boundary. g_{part} and g_{sub} are the fractions of particles and subboundary junctions where cavitation takes place. The averaging over different orientations gives the factor 0.9. Equation (11.31) has been verified successfully by comparison to experiments for austenitic stainless steels [11] and copper [33].

A 1Cr0.5Mo ferritic-bainitic steel will be used to illustrate cavitation during LCF [17, 18]. Some of the specimens were creep tested before the LCF to study the

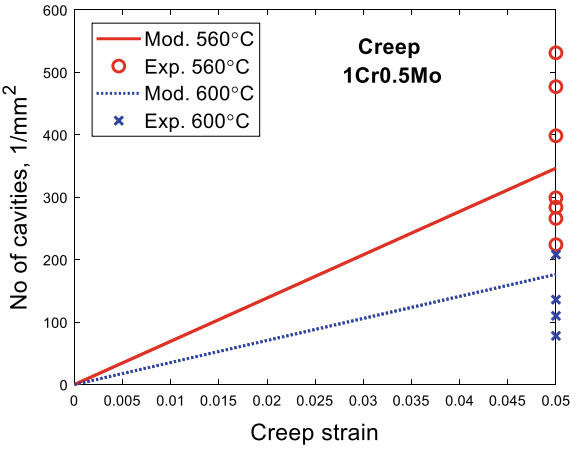

Fig. 11.13 Number of cavities versus creep strain for specimens later used in LCF testing. Experimental data from [17] are compared with the model in Eq. (11.31). Redrawn from [18] with permission of Taylor & Francis

combined influence of creep and cycling. The creep testing was performed at a stress of 100 MPa and was terminated when a creep strain of 5% was reached. The creep testing temperatures were 560 and 600 °C. The amount of cavitation is illustrated in Fig. 11.13.

The cavities are assumed to be nucleated around the carbides in the grain boundaries. By comparing the distribution of cavities and particles in the grain boundaries at 560 °C where micrographs are available, it turns out that one particle out of 5 initiated a cavity. This means that g_{part} is 0.2. It is not possible to predict the value of g_{part}. The grain size d_{grain} was 12 μm and the creep exponent $n_N = 4.4$. Equation (11.30) then gives a C_s value of 2.5×10^{-6} m. These parameter values are used in the modeling also for LCF.

The nucleation rate at 600 °C is clearly lower than at 560 °C. This has been interpreted as a result of particle coarsening. Since no basic creep model is available for the 1Cr0.5Mo steel, the amount of coarsening has to be estimated indirectly. With the help of Norton equations, the creep rates $\dot{\varepsilon}_{560}$ at 560 and $\dot{\varepsilon}_{600}$ at 600 °C can be expressed as

$$\dot{\varepsilon}_{560} = A_N \exp(-Q_{creep}/R_G T_{560})(\sigma - \sigma_{p560})^{n_N} \tag{11.32}$$

$$\dot{\varepsilon}_{600} = A_N \exp(-Q_{creep}/R_G T_{600})(\sigma - \sigma_{p600})^{n_N} \tag{11.33}$$

Since the creep rates have been measured, their ratio 21.3 is known. Since also the activation energy $Q_{creep} = 290$ kJ/mol and the stress exponent $n_N = 4.4$ are known, the ratio between the particle strengths σ_{p560} and σ_{p600} at 560 and 600 °C can be determined from Eqs. (11.32) and (11.33). It is found that the particle strengthening at 600 °C is 70% of that at 560 °C. Assuming that this is a consequence of differences in particle spacing according to model in Sect. 7.3, the corresponding differences in nucleation rate can be estimated. These results are applied in Fig. 11.13. It can be

seen that the observations for a creep strain of 0.05 can be reproduced in a reasonable way.

In [17] LCF tests with and without a hold time in tension were carried out at 535 °C. The length of the hold time was 5 min. Some of the tests were exposed to static creep before LCF as described above. The number of cavities was recorded before and after LCF. Only tests with a hold time significantly influenced the number of creep cavities. For this reason, the analysis will be focused on the tests with hold times. Seven such tests were performed. Some data for these tests can be found in Table 11.1.

The six left most columns in Table 11.1 give experimental data for the tests: total strain range ε_{tot}, stress range σ_{range}, number of cycles to failure N_{cycl}, number of cycles to crack initiation N_{init}, and the number of measured cavities per unit area n_{cav} after the test. Properties for the loops have been computed with the model in Sect. 11.3.1. Results are presented in the four right most columns in Table 11.1: stress drop due to relaxation during the hold time $\Delta\varepsilon_{hold}$, amount of creep strain during the hold time $\Delta\varepsilon_{hold}$, amount of creep strain during the tension going part of the cycle $\Delta\varepsilon_{cr\_tens}$ (excluding the strain during the hold time), and amount of creep strain during the compression going part of the cycle $\Delta\varepsilon_{cr\_cmpr}$. The stress relaxation during the hold time varies from 50 to 90 MPa. The corresponding creep strain lies between 0.00038 and 0.00067. The amounts of creep strain in the compression and tension going part of the cycle are almost two orders of magnitude smaller. Only the first of these four quantities can be compared with the experimental data. It was demonstrated in Sect. 11.3.2 that this could be accomplished in a successful way.

It is assumed that amount of cavitation during cycling can be based on Eq. (11.31), i.e. on the total creep strain. The total creep strain is the amount of creep strain in each cycle multiplied by the number of cycles N_{cycl}. There are three contributions to the creep strain in each cycle: (i) during the hold time $\Delta\varepsilon_{hold}$, (ii) during the compression going part of the cycle $\Delta\varepsilon_{cr\_cmpr}$ and (iii) during the tension going part $\Delta\varepsilon_{cr\_tens}$. These contributions are directly added. The result is the following expression for the number of cavities n_{cav}

$$n_{cav} = B_s(1 - f_{close})(\Delta\varepsilon_{hold} + \Delta\varepsilon_{cr\_tens} + \Delta\varepsilon_{cr\_cmpr})N_{cycl} \tag{11.34}$$

The total creep strain in each cycle is the expression within brackets in Eq. (11.34). The main part of the creep strain appears during the hold time. $\Delta\varepsilon_{cr\_tens}$ and $\Delta\varepsilon_{cr\_cmpr}$ are much smaller. In addition they have opposite signs so they cancel each other to a significant extent. In cycles with hold time in tension, the absolute value of $\Delta\varepsilon_{cr\_cmpr}$ is larger than that of $\Delta\varepsilon_{cr\_tens}$ so the overall effect is that the creep during the hold time is marginally reduced in the remainder of the cycle. The creep strain is multiplied by the B_s constant, Eq. (11.31). Some cavities may close during the compression going part of the cycle. This is taken into account with the help of the constant f_{close} which is the fraction of cavities that are closed in each cycle. The value of f_{close} will be estimated in Sect. 11.4.2.

Table 11.1 Data for hysteresis loops with hold time for 1Cr0.5Mo (Reprinted from [17] with permission of Taylor & Francis)

Pre-creep	ε_{tot}, %	σ_{range} MPa	N_{cycl}	N_{init}	n_{cav} 1/mm^2	$\Delta\sigma_{hold}$ MPa	$\Delta\varepsilon_{hold} \times 10^{-2}$%	$\Delta\varepsilon_{cr\_tens} \times 10^{-4}$%	$\Delta\varepsilon_{cr\_cmpr} \times 10^{-4}$%
No	0.92	590	720	540	905	62	4.5	6.2	−8.2
No	0.64	559	1590	1283	1097	52	3.8	2.8	−4.4
No	1.2	655	490	348	173	86	6.3	9.7	−13
No	1.53	669	409	334	1156	91	6.7	14	−18
Yes	0.55	447	1710	1489	3202	60	4.4	4.3	−6.5
Yes	0.83	494	671	568	3359	79	5.8	9.1	−14
Yes	1.11	502	576	517	2233	82	6.0	15	−21

The application of Eq. (11.34) is compared to experimental data in Figs. 11.14 and 11.15. The difference between the Figures is that in Fig. 11.15, the specimens were exposed to creep before the LCF testing.

For the modeling the same values as in Fig. 11.13 have been used with $C_s = 2.5\ \mu m$ and $d_{grain} = 12\ \mu m$. The subgrain size d_{sub} was determined at the average stress in the tension and compression going part of the cycles. The resulting values

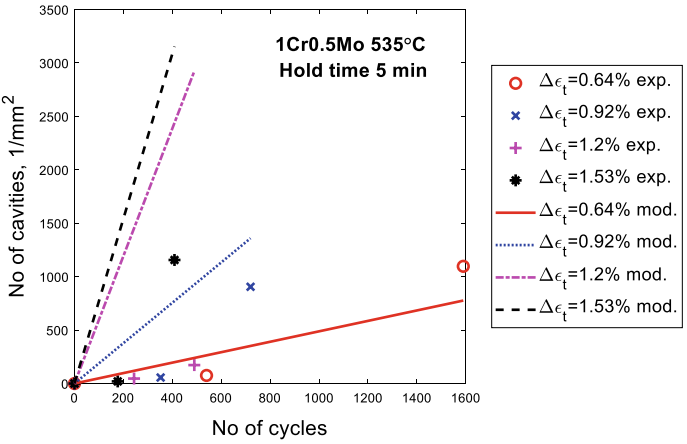

Fig. 11.14 Number of cavities versus number of cycles after LCF testing of 1Cr0.5Mo steels at 535 °C with 5 min hold time in the cycle. Total strain ranges between 0.64 and 1.53%. Experimental data from [17] are compared with the model in Eq. (11.34). Redrawn from [18] with permission of Taylor & Francis

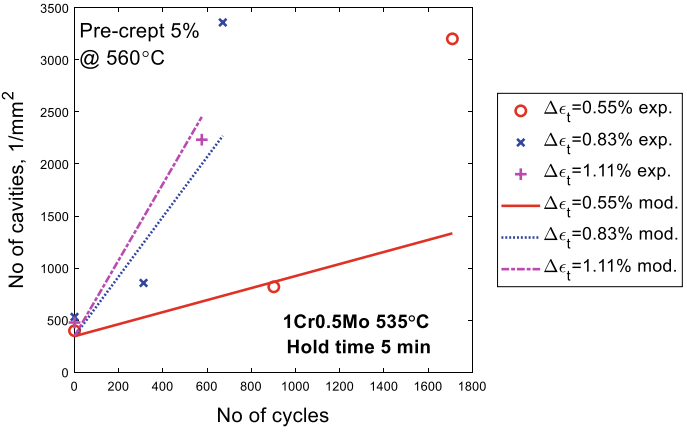

Fig. 11.15 Number of cavities versus number of cycles after LCF testing of 1Cr0.5Mo steels at 535 °C with 5 min hold time in the cycle. Total strain ranges between 0.55 and 1.11%. The specimens were exposed to 5% creep strain before the LCF testing. Experimental data from [17] are compared with the model in Eq. (11.34). Redrawn from [18] with permission of Taylor & Francis

are about $d_{sub} = 2$ μm. In Fig. 11.15, the number of cavities from the pre-creep in Fig. 11.13 has been added to the results. It seems that the cavitation model gives an acceptable result for most of the specimens.

11.4.2 Cavity Growth

Already in the 1950ties, Hull and Rimmer derived an expression for diffusion controlled growth of creep cavities. The expression was later modified by several authors to give it a more practical form. For example, Beere and Speight [34] derived the following formula that is of the form commonly used today, Eq. (10.11)

$$\frac{dR_{cav}}{dt} = 2D_0K_f(\sigma - \sigma_0)\frac{1}{R_{cav}^2} \tag{11.35}$$

where R_{cav} is the cavity radius in the grain boundary plane, dR_{cav}/dt its growth rate, σ_0 the sintering stress, $2\gamma_s \sin(\alpha)/R_{cav}$, where γ_s is the surface energy of the cavity per unit area and α the cavity tip angle. If the cavities are sufficiently small, they will shrink rather than grow after nucleation. The sintering stress avoids that the formula predicts growth in such cases. D_{GB} the grain boundary self-diffusion coefficient, and Ω_a the atomic volume are combined into a grain boundary diffusion parameter D_0, $D_0 = \delta D_{GB}\Omega_a/k_BT$. k_B is the Boltzmann's constant and T the absolute temperature. $K_f \approx 0.1$ is approximately a constant.

As discussed in Sect. 10.5, Eq. (11.35) typically overestimates the growth rates during creep. This problem was solved by introducing the requirement that the growth rate should not be higher than the creep rate of the surrounding matrix. This is referred to as constrained growth [12]. This means that equilibrium is established between the cavity growth and the creep deformation. Without this condition, the growth is referred to as unconstrained, and the growth rate in this case is given by Eq. (11.35). However, it is difficult to imagine that equilibrium can be established during the short cycle time and the small creep strain in common LCF tests. As illustrated in Table 11.1, the creep strains in each cycle are quite small. It must be assumed that unconstrained growth applies in LCF.

In addition for diffusion, plastic deformation can also give rise to growth of creep cavities. This was discussed in Sect. 10.5.3. A model where the cavity growth is proportional to the amount of grain boundary sliding (GBS) will be used [5], Eq. (10.24)

$$R_{cav} = C_s\varepsilon \tag{11.36}$$

Again the constant C_s is given by Eq. (11.30). After nucleation for example around particles, the cavities can continue to expand due to GBS. Elongated creep cavities in grain boundaries are often observed. It was demonstrated in Fig. 10.10

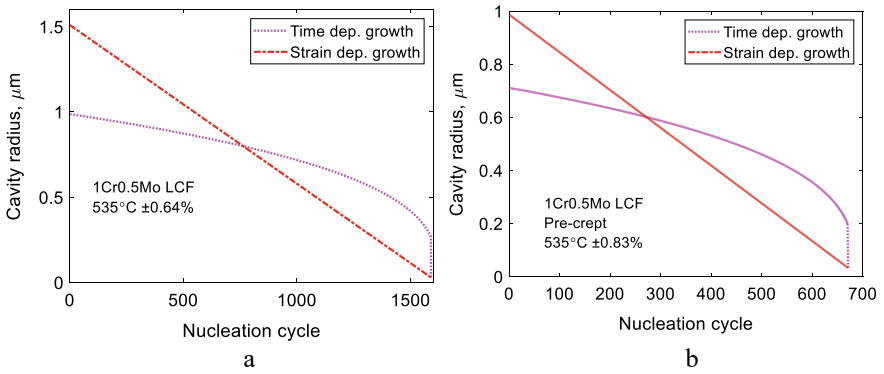

Fig. 11.16 Cavity radius versus the cycle where the cavity was nucleated. Two examples from the tests in Table 11.1 for 1Cr0.5Mo steel. Model values for diffusion controlled growth according to Eq. (11.35) and strain controlled growth, Eq. (11.36). Redrawn from [18] with permission of Taylor & Francis

that Eq. (11.36) could describe cavity growth for a 12CrMo steel and an austenitic stainless steel TP347 (17Cr12NiNb).

Equations (11.35) and (11.36) are applied in Fig. 11.16 to two cases in Table 11.1 for the 1Cr0.5Mo steel.

Figure 11.16 illustrates how a distribution of cavity sizes is obtained. The cavities that are nucleated early are larger since they are more exposed to growth processes. The two types of growth mechanisms give different behavior as a function of initiation cycle. Diffusion growth shows a rapid increase in cavity radius initially and a slower growth later. Strain controlled growth on the other hand has a constant increase with cycle number. No detailed measurement of the cavity size was performed in [17]. This would have been difficult anyway since the specimens were etched. Taking this into account, the computed cavity radii are consistent with the observations.

In the case of constrained growth, the values from diffusion and strain controlled growth should definitely not be added since the two mechanisms give each the maximum possible growth rates. This was discussed in Sect. 10.5.3. However, for unconstrained growth this conclusion is no longer self-evident. However, it turns out in the studied cases for 1Cr0.5Mo that if the two contributions are added quite large cavity radii of up to 10 μm are obtained which is not in agreement with observations. Adding the two contributions should therefore be avoided.

Equation (11.35) should in principle be possible to use to estimate the fraction of cavities that are closed during the compression going part of the LCF cycle. If it is applied directly it does not work. This can be seen in the following way. According to Eq. (11.36), in the first cycle a cavity with a radius of about 1×10^{-9} m is formed. With Eq. (11.35), such a cavity would disappear in fractions of a second. As a consequence, no cavities would be formed contrary to the observations. To make the result sensible, another case has to be considered. It is possible that the GBS does not take place in each cycle but occurs stepwise. It has been shown for copper during

static creep that the nucleated cavity size is in accordance with [33]

$$R_{\text{cavmin}} = 2\gamma_s \sin(\alpha)/\sigma \tag{11.37}$$

This relation is obtained by putting $\sigma = \sigma_0$ in Eq. (11.35). For the 1Cr0.5Mo steel, R_{cavmin} is about 1.5×10^{-8} m. With a strain rate of 0.003/s, in the compression part the cycle time is about 3 s. Using Eq. (11.35) one can derive that cavities that are smaller than about $R_{\text{cavmin}}/2.5$ are dissolved during this time. If it is assumed that the formed cavities have initially a size in the interval 0–2 R_{cavmin}, about a fifth of the cavities are closed during the compression part of the cycle. If this value is representative, f_{close} in Eq. (11.34) would be 0.2. However, this value is uncertain and it has not been applied in the computation of the nucleation rate in Figs. 11.14 and 11.15.

11.5 Summary

- Many plants that are operating at high temperatures are exposed to both creep and fatigue. A number of fossil-fired plants are running under intermittent loading while in the past they were adapted to base loading. The reason is that renewable sun and wind units do not supply power continuously and have to be backed up by conventional plants. As a consequence, fossil-fired power plants experience often combined creep and fatigue loading nowadays.
- Numerous empirical methods are available for assessing the material damage in plants. The classical Robinson's and Miner's damage summation rules have been extensively tested. Some results suggest that the damage typically can vary from being underestimated by a factor of three to being overestimated by the same factor. From a practical point of view such a large uncertainty is not acceptable. To base damage assessment just on mechanical properties is consequently difficult. It is also important to analyze the changes in the microstructure such as particle and substructure coarsening and formation of creep cavities and compare these findings with models. In this respect continuum damage mechanics can be quite useful.
- Many empirical models for damage assessment can predict both the development of mechanical properties and the microstructure. However, as for all empirical models, they have to be adapted to specific cases to give meaningful results. The alternative is to use basic models for both mechanical properties and microstructure. Such models are readily available also for the development of the microstructure as described in this book. Although basic models are somewhat more complex to program, the predictions are far safer.
- For analyzing creep damage, the assessment of cavitation has been quite useful. In recent years basic quantitative models for cavitation have been established that are directly applicable in this context. However, the situation has been different for cyclic loading. Two essential features have been missing. Prediction of stress

strain loops has been based on empirical approaches meaning that the results are restricted to the experimental case(s) under investigation. It is demonstrated in this chapter that many of the basic models applied in non-cyclic situations can be transferred to cyclic cases. The main parameter that has to be changed is the dynamic recovery constant. The reason for this is simple. During cyclic deformation dislocations encounter each other much more frequently than in monotonous cases and it increases the rate of recovery. Therefore, the recovery constant must take a higher value.

- The other missing feature has been the absence of models for the development of cavitation. It is expected that cavitation plays the same important role during creep-fatigue interaction as during plain creep. With the help of the models for the stress strain loops, the amount of creep strain in each cycle can be computed. By applying this in the formula for cavity nucleation, the number of cavities after LCF and after combined creep and LCF for a 1Cr0.5Mo steel have been possible to compute in an acceptable way.
- The cavity growth rate for the 1Cr0.5Mo steel has also been analyzed. Both models for diffusion controlled and strain controlled growth have been considered. Since quite small creep strains appear in each cycle unconstrained diffusion growth has been used. The reason is that it is assumed to be unrealistic that equilibrium between the cavity growth and the creep deformation could be established. The strain controlled growth is based on the assumption that the amount of growth is equal to the amount of grain boundary sliding. This assumption has previously worked well for two steels during creep where data are available. Although the diffusion growth is faster initially, the total growth is about the same as for strain controlled growth of the 1Cr0.5Mo steel. The final cavity size is in the interval from 0.1 to 1 μm, which seems reasonable. These results should be considered as tentative since detailed experiments are not available.
- It is often assumed that some closure of cavities takes place during the compression part of the load cycle. With the help of the model for diffusion controlled growth, it should in principle be possible to predict the amount of closure. Unfortunately, meaningful results are not obtained unless special assumptions are made. Therefore, the amount of cavity closure remains an open issue. In the prediction of cavity nucleation for 1Cr0.5Mo, no account of cavity closure has been taken into account. Satisfactory predictions have been obtained anyway indicating that the amount of cavity closure must be limited.

References

1. D.A. Miller, R.H. Priest, E.G. Ellison, Review of material response and life prediction techniques under fatigue-creep loading conditions. High Temp. Mater. Process. (London) **6**, 155–194 (1984)
2. S. Holdsworth, Creep-fatigue interaction in power plant steels. Mater. High Temp. **28**, 197–204 (2011)

3. L. Lundberg, R. Sandstrom, Application of low cycle fatigue data to thermal fatigue cracking. Scand. J. Metall. **11**, 85–104 (1982)
4. J.J. Moverare, A. Sato, S. Johansson, M. Hasselqvist, R.C. Reed, J. Kanesund, K. Simonsson, On localized deformation and recrystallization as damage mechanisms during thermomechanical fatigue of single crystal nickel-based superalloys, in *Advanced Materials Research* (2011), pp. 357–362
5. R. Sandström, Basic creep-fatigue models considering cavitation. Trans. Indian Natl. Acad. Eng. **7**(2), 583–591 (2021)
6. R. Sandström, J. He, Survey of creep cavitation in fcc metals, in *Study of Grain Boundary Character* (inTech, 2017), pp. 19–42
7. S.R. Holdsworth, Creep-fatigue properties of high temperature turbine steels. Mater. High Temp. **18**, 261–265 (2001)
8. L.C. Lim, Cavity nucleation at high temperatures involving pile-ups of grain boundary dislocations. Acta Metall. **35**, 1663–1673 (1987)
9. D. McLean, M.H. Farmer, The relation during creep between grain-boundary sliding, subcrystal size, and extension. J. Inst. Met. **85**, 41–50 (1957)
10. R. Sandström, R. Wu, Influence of phosphorus on the creep ductility of copper. J. Nucl. Mater. **441**, 364–371 (2013)
11. J. He, R. Sandström, Formation of creep cavities in austenitic stainless steels. J. Mater. Sci. **51**, 6674–6685 (2016)
12. B.F. Dyson, Constraints on diffusional cavity growth rates. Metal Sci. **10**, 349–353 (1976)
13. J.R. Rice, Constraints on the diffusive cavitation of isolated grain boundary facets in creeping polycrystals. Acta Metall. **29**, 675–681 (1981)
14. J. He, R. Sandström, Creep cavity growth models for austenitic stainless steels. Mater. Sci. Eng. A **674**, 328–334 (2016)
15. R. Sandström, J.-J. He, Prediction of creep ductility for austenitic stainless steels and copper. Mater. High Temp. **39**(6), 427–435 (2022)
16. J. He, R. Sandström, Basic modelling of creep rupture in austenitic stainless steels. Theoret. Appl. Fract. Mech. **89**, 139–146 (2017)
17. J. Storesund, R. Sandstrom, Interaction of creep damage and low cycle fatique damage in a 1Cr0.5Mo steel. Isij Int. **30**, 875–884 (1990)
18. R. Sandström, Cavitation during creep-fatigue loading. Mater. High Temp. **40**, 174–183 (2023)
19. D.R. Hayhurst, Creep rupture under multi-axial states of stress. J. Mech. Phys. Solids **20**, 381–382 (1972)
20. J.-F. Wen, S.-T. Tu, F.-Z. Xuan, X.-W. Zhang, X.-L. Gao, Effects of stress level and stress state on creep ductility: evaluation of different models. J. Mater. Sci. Technol. **32**, 695–704 (2016)
21. F.K.G. Odqvist, *Mathematical Theory of Creep and Creep Rupture* (Clarendon Press, 1966)
22. J.-F. Wen, S.-T. Tu, A multiaxial creep-damage model for creep crack growth considering cavity growth and microcrack interaction. Eng. Fract. Mech. **123**, 197–210 (2014)
23. R.P. Skelton, H.J. Maier, H.J. Christ, The Bauschinger effect, Masing model and the Ramberg-Osgood relation for cyclic deformation in metals. Mater. Sci. Eng. A **238**, 377–390 (1997)
24. S.R. Holdsworth, Creep-fatigue crack growth from a stress concentration. Mater. High Temp. **15**, 111–116 (1998)
25. R. Sandström, Fundamental models for the creep of metals, in *Creep* (inTech, 2017)
26. R. Sandström, J. Hallgren, The role of creep in stress strain curves for copper. J. Nucl. Mater. **422**, 51–57 (2012)
27. R. Sandstrom, Basic model for primary and secondary creep in copper. Acta Mater. **60**, 314–322 (2012)
28. F. Sui, R. Sandström, Basic modelling of tertiary creep of copper. J. Mater. Sci. **53**, 6850–6863 (2018)
29. H.C.M. Andersson, R. Sandstrom, D. Debord, Low cycle fatigue of four stainless steels in 20% CO-80% H-2. Int. J. Fatigue **29**, 119–127 (2007)
30. Data sheets on the elevated-temperature properties of normalized and tempered 1Cr-0.5Mo steel plates for pressure vessels (SCMT 2 NT) National Research Institute for Metals Tokyo, Japan (2002)

31. R. Sandstrom, H.C.M. Andersson, Modelling of hysteresis loops during thermomechanical fatigue, in *ASTM Special Technical Publication* (2003), pp. 31–44
32. F. Ghahremani, Effect of grain boundary sliding on steady creep of polycrystals. Int. J. Solids Struct. **16**, 847–862 (1980)
33. Y. Das, A. Fernandez-Caballero, E. Elmukashfi, H. Jazaeri, A. Forsey, M.T. Hutchings, R. Schweins, P.J. Bouchard, Stress driven creep deformation and cavitation damage in pure copper. Mater. Sci. Eng. A **833** (2021)
34. W. Beere, M.V. Speight, Creep cavitation by vacancy diffusion in plastically deforming solid. Metal Sci. **21**, 172–176 (1978)

Open Access This chapter is licensed under the terms of the Creative Commons Attribution 4.0 International License (http://creativecommons.org/licenses/by/4.0/), which permits use, sharing, adaptation, distribution and reproduction in any medium or format, as long as you give appropriate credit to the original author(s) and the source, provide a link to the Creative Commons license and indicate if changes were made.

The images or other third party material in this chapter are included in the chapter's Creative Commons license, unless indicated otherwise in a credit line to the material. If material is not included in the chapter's Creative Commons license and your intended use is not permitted by statutory regulation or exceeds the permitted use, you will need to obtain permission directly from the copyright holder.